Orthorhombic $BiFeO_3$

J. C. Yang,[1] Q. He,[2,3] S. J. Suresha,[4] C. Y. Kuo,[5,6] C. Y. Peng,[1] R. C. Haislmaier,[7] M. A. Motyka,[8] G. Sheng,[7] C. Adamo,[9] H. J. Lin,[5] Z. Hu,[6] L. Chang,[1] L. H. Tjeng,[6] E. Arenholz,[3] N. J. Podraza,[10] M. Bernhagen,[11] R. Uecker,[11] D. G. Schlom,[9,12] V. Gopalan,[7] L. Q. Chen,[7] C. T. Chen,[5] R. Ramesh,[2] and Y. H. Chu[1,*]

[1]*Department of Materials Science and Engineering, National Chiao Tung University, Hsinchu 300, Taiwan*
[2]*Department of Physics, University of California, Berkeley, California 94720, USA*
[3]*Advanced Light Source, Lawrence Berkeley National Laboratory, Berkeley, California 94720, USA*
[4]*National Center for Electron Microscopy, Lawrence Berkeley National Laboratory, Berkeley, California 94720, USA*
[5]*National Synchrotron Radiation Research Center, Hsinchu 30076, Taiwan*
[6]*Max-Planck Institute for Chemical Physics of Solids, Nöthnitzer Straβe 40, 01187 Dresden, Germany*
[7]*Department of Materials Science and Engineering, Pennsylvania State University, University Park, Pennsylvania 16802, USA*
[8]*Department of Engineering Science and Mechanics, Pennsylvania State University, University Park, Pennsylvania 16802, USA*
[9]*Department of Materials Science and Engineering, Cornell University, Ithaca, New York 14853, USA*
[10]*Department of Physics and Astronomy, University of Toledo, Toledo, Ohio 43606, USA*
[11]*Leibniz Institute for Crystal Growth, Max-Born-Straβe 2, D-12489 Berlin, Germany*
[12]*Kavli Institute at Cornell for Nanoscale Science, Ithaca, New York 14853, USA*

(Received 3 July 2012; revised manuscript received 7 September 2012; published 14 December 2012)

A new orthorhombic phase of the multiferroic $BiFeO_3$ has been created via strain engineering by growing it on a $NdScO_3(110)_o$ substrate. The tensile-strained orthorhombic $BiFeO_3$ phase is ferroelectric and antiferromagnetic at room temperature. A combination of nonlinear optical second harmonic generation and piezoresponse force microscopy revealed that the ferroelectric polarization in the orthorhombic phase is along the in-plane $\langle 110\rangle_{pc}$ directions. In addition, the corresponding rotation of the antiferromagnetic axis in this new phase was observed using x-ray linear dichroism.

DOI: 10.1103/PhysRevLett.109.247606 PACS numbers: 77.55.Nv, 75.85.+t, 77.80.bn

Multiferroics possess simultaneous electric and magnetic order parameters and the potential to manipulate one through the other [1]. Motivated by potential applications and fundamental understanding, the single-phase, room-temperature multiferroic $BiFeO_3$ (BFO) has played a key role in rejuvenating this field [2–6]. Recently, a strain driven isosymmetric phase transition has been demonstrated in this material system [7]. Experimentally, tetragonal, strained rhombohedral, and mixed-phase BFO thin films have been created and widely studied to show enhanced either piezo- or ferroelectricity or magnetism. Triggered by this, several theoretical predictions suggest a rich strain-temperature phase diagram composing phases with different symmetries [7,8]. In this study, we start from phase-field modeling to provide an extended scenario of the BFO phase diagram, specifically under biaxial tensile stress imposed through a lattice mismatched substrate. In conjunction with experimental data, we demonstrate the existence of an orthorhombic phase in epitaxial films subjected to such stresses.

We employed the same material constants [9] of BFO and computational approach as described in our previous work [10]. The domain stability of a $(001)_{pc}$ BFO thin film under tensile biaxial constraint is calculated via phase-field simulations, and the predicted strain-temperature phase stability diagrams with short-circuit and open-circuit boundary conditions are shown in Figs. 1(a) and 1(b), respectively. In both diagrams, the stable phases are labeled as cubic paraelectric, distorted rhombohedral (R), orthorhombic (O), and the mixture of R and O phases ($R + O$). In order to obtain the phase stability and phase boundaries, the spatial distribution of the polarization field is determined by numerically solving the time-dependent Ginzburg-Landau equations [11]. We use a background dielectric constant $\kappa = 10$ in the calculation [12]; for the open-circuit diagram in Fig. 1(b), the phase boundary predicted from the vacuum dielectric constant of 1 is also presented for comparison.

As shown in Figs. 1(a) and 1(b), the electric boundary condition has a significant impact on the distorted rhombohedral-orthorhombic phase boundary for BFO thin films. Figure 1(a) shows that the distorted rhombohedral

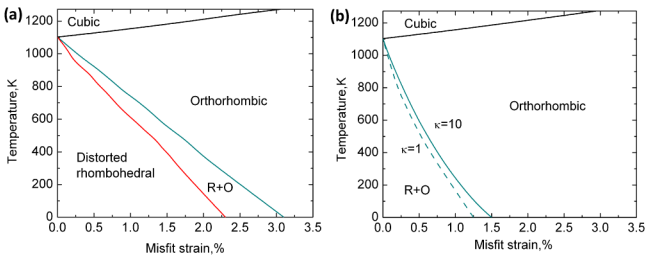

FIG. 1 (color online). Strain-temperature phase diagrams of $BiFeO_3$ thin film from phase-field simulations. (a) Under short-circuit boundary condition and (b) under open-circuit boundary conditions.

phase transforms to the orthorhombic phase at ~1.7% tensile strain at room temperature (300 K), and the pure orthorhombic phase cannot be stabilized until the strain magnitude is higher than ~2.2%. This short-circuit diagram is essentially the same as the tensile part of the previous reported diagram [7].

The open-circuit boundary condition leads, however, to a dramatically different phase diagram [Fig. 1(b)]. The depolarization field suppresses the out-of-plane (OOP) polarization and promotes the formation of orthorhombic domains, leading to a mixture of distorted rhombohedral and orthorhombic phases even at zero misfit strain. For comparison, we also calculated the phase boundary assuming the dielectric constant of vacuum in the electrostatic equation. The depolarization field effect plays an important role in mediating the phases of BFO thin films under tensile strains. Although we observe a larger depolarization field effect, both results demonstrate that BFO with approximately ~1.0% tensile strain exhibits an orthorhombic phase at room temperature. We also performed additional phase-field simulations [13] by constructing a thermodynamic potential assuming the distorted rhombohedral to orthorhombic phase boundary at 8% tensile strain at 0 K, based on a recent density function calculation reported by Dupé *et al.* [14]. This modified potential leads to a mixture of orthorhombic and distorted rhombohedral phase under the open-circuit boundary condition for BFO with 1.0% strain.

To assess the validity of the strain phase diagrams in Fig. 1, BFO films were prepared on substrates that impart biaxial strain due to epitaxial mismatch. In this study, we synthesized 15 nm thick epitaxial BFO thin films on orthorhombic $NdScO_3(110)_o$ (NSO, with pseudocubic spacing 4.01 Å) [15] substrates, which provides ~1.1% in-plane (IP) tensile strain, via pulsed laser deposition at 700 °C in an oxygen pressure of 1×10^{-1} Torr and cooled in 1 atm of oxygen. Their commensurate nature was confirmed by four-circle x-ray diffraction. X-ray diffraction $\theta - 2\theta$ scans of all of the samples studied (from 15° to 100° using Cu K_α radiation, not shown here) exhibited only peaks attributable to the epitaxial growth of a phase-pure perovskite film.

The quality of BFO films prepared by pulsed laser deposition and its crystal structure were characterized via transmission electron microscopy (TEM) and high-resolution x-ray reciprocal space mapping (RSM). To avoid possible confusion arising from the index transformation, we refer $[001]_o$, $[1\bar{1}0]_o$, and $[110]_o$ directions in the orthorhombic system to the $[100]_{pc}$, $[010]_{pc}$, and $[001]_{pc}$ directions in the pseudocubic system. High angle annular dark field scanning TEM images and the corresponding fast Fourier transforms (FFT) [Fig. 2(a)] obtained from a $(010)_{pc}$ cross section reveal the high quality of the epitaxial BFO layer. Analysis of the FFT pattern [inset of Fig. 2(a)] with pseudocubic indices yields an in-plane parameter of 4.0 Å and an out-of-plane parameter of 3.90 Å, which results from the tensile constraint exerted by the substrate lattice. This confirms epitaxial growth and a 0.975 c/a ratio in the tensile strained BFO; the FFT pattern and the suppressed c/a ratio imply an orthorhombic symmetry. Furthermore, direct observation of the domain boundaries in plan-view TEM images [Fig. 2(b)] reveal stripelike contrast, reflecting the anisotropic lattice structure in such a tensile strained BFO. For further confirmation, RSMs were obtained from two incident directions with respect to the NSO substrate: one has the incident x-ray parallel to $[100]_{pc}$ [Fig. 3(a)], and the other is parallel to $[010]_{pc}$ [Fig. 3(b)]. The coordinate axis, q_i, represents the i-axis component of the reciprocal space vector. Both symmetric RSM (003_{pc} reflections) and asymmetric RSMs (103_{pc} and 013_{pc}) are measured for depiction of the whole structure. In the $[100]_{pc}$ incidence, RSM reveals a "dragonflylike" set comprising four peaks in each map (labeled as 1–8). Peaks labeled as 4 and 8 come

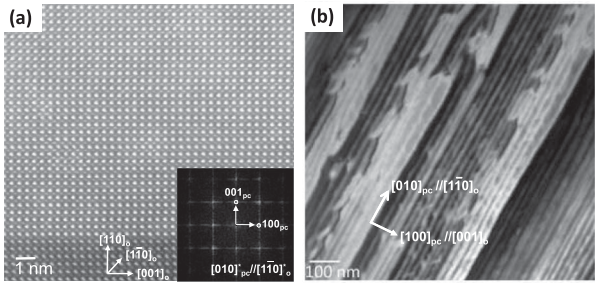

FIG. 2. TEM micrographs of a $BiFeO_3$ thin film on $NdScO_3$. (a) High angle angular dark field STEM image of the $BiFeO_3/NdScO_3$ interface of a 15 nm thick film and corresponding Fourier transforms of the film (inset) indexed with pseudocubic indices. (b) Planar-view image showing the striped domain pattern in the 15 nm thick film.

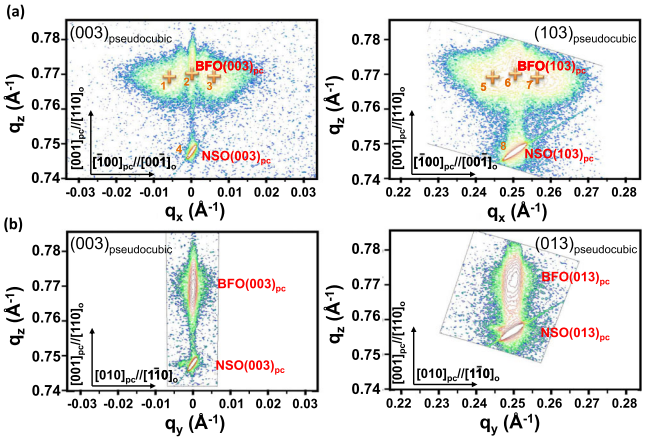

FIG. 3 (color online). X-ray reciprocal space mapping studies of a $BiFeO_3$ thin film on $NdScO_3$. Symmetric and asymmetric reciprocal space maps of $BiFeO_3$ and $NdScO_3$ with the incident x-ray beam along (a) $[100]_{pc}$ and (b) $[010]_{pc}$ directions. Corresponding $BiFeO_3$ and $NdScO_3$ main peaks are also labeled with pseudocubic indexes.

from the NSO substrate and the peaks of 1, 2, 3 and 5, 6, 7 are all ascribed to the BFO film. At first glance, it is intriguing to note the split peaks (labeled as 1, 3 and 5, 7) of BFO, which usually result from tilted crystal structures or satellite reflections of the periodic domain structures. Detailed q_x-scan measurements have been employed to reveal the origin of the splitting (see the Supplemental Material [16], Fig. S1). These studies show that the length of the splitting remains the same (namely, $\Delta q_x = 0.006$ for all the (00L) BFO reflections) irrespective of the reciprocal plane spacing. Comparing both the experimental and simulation results leads us to the conclusion that the split peaks are caused by the satellite reflection arising from the periodic domain structures (~ 16 nm average lateral size of the stripe domain). We found that the $(003)_{pc}$ peaks of BFO are well aligned at $q_z \sim 0.77$ Å^{-1}, and all spots for BFO and NSO appear at virtually the same q_x and q_y in-plane interplanar spacing. These indicate that both the in-plane interplanar lattice parameters of the BFO film and the NSO substrate are very close to each other. The lattice parameters of this structure are calculated to be $a \sim 3.99$ Å, $b \sim 4.00$ Å, and $c \sim 3.89$ Å for BFO. By comparing both symmetrical and asymmetrical RSM results, we conclude that this phase possesses $\beta = \gamma = 90°$ structure; moreover, it shows an offset tilting angle from the $[001]_{pc}$ substrate normal by $\sim 0.63°$ along the $[010]_{pc}$ directions.

Having established that BFO grown on NSO substrates shows a distorted orthorhombic structure, we now turn to investigate the correlation of structural symmetry and polarization. Herein, the linear and nonlinear optical properties of the orthorhombic (O) phase BFO thin film are presented. Linear optical properties of BFO with different structures were obtained from room temperature ellipsometric spectra; see the Supplemental Material [16], Fig. S2. A similar approach has been used to interpret the structural strain and local symmetry breaking [17].

To determine the point group symmetry of the BFO/NSO film, nonlinear optical second harmonic generation (SHG) was used, which is a domain symmetry-sensitive technique for polar materials. SHG is a process whereby two photons of frequency ω are converted into one photon of frequency 2ω by a nonlinear medium through the creation of a nonlinear polarization, $P_i^{2\omega} = d_{ijk} E_j^{\omega} E_k^{\omega}$, where d_{ijk} is the nonlinear optical tensor and $E_{j,k}^{\omega}$ is the fundamental electric field. While the observation of SHG indicates the existence of a polar phase, the anisotropy of the SHG signal can reveal the point group symmetry of a material [18]. SHG experiments were performed on BFO/NSO thin film with an 800 nm fundamental beam (Ti: sapphire laser, 80 fs pulses, 1 kHz repetition rate). The experimental geometry is shown in Fig. 4(a). Based on the TEM data, we consider an orthorhombic, $mm2$ (with $\{001\}_{pc}$ and $\{110\}_{pc}$ mirror planes), model structure where we assume the polar direction of the four possible domain variants are along the $\langle 110\rangle_{pc}$ directions, shown as light

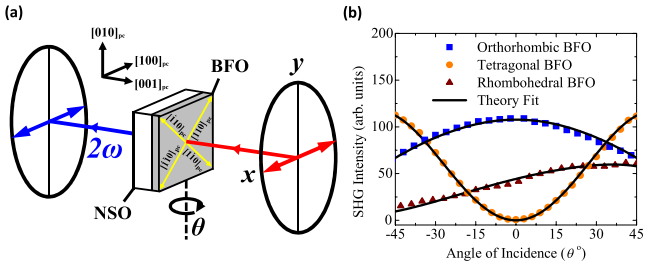

FIG. 4 (color online). Nonlinear optical second harmonic generation of orthorhombic $BiFeO_3$. (a) The experimental geometry for SHG tilt scans with the incident electric field and detected SHG both along the x direction. The four possible polarization variants are shown as gray (yellow) lines on the BFO film surface along the $\langle 110\rangle_{pc}$ directions. (b) Tilt scans showing SHG intensity as a function of incidence angle (θ) for orthorhombic $(001)_{pc}$ $BiFeO_3/(110)_o$ $NdScO_3$ (blue squares), rhombohedral $(111)_{pc}$ $BiFeO_3/(111)_{pc}$ $SrTiO_3$ (red triangles), and tetragonal $(001)_{pc}$ $BiFeO_3/(110)_o$ $YAlO_3$ (orange circles), with the corresponding theory fits shown in black lines.

gray (yellow) arrows on the surface in Fig. 4(a). If the polarization lies in the plane of the film as predicted [14], the SHG signal will have maximum intensity at normal incidence ($\theta = 0°$) since the fundamental electric field will sample the largest polarization component in this configuration. If the sample is rotated about the y axis, the SHG signal should decrease symmetrically about normal incidence. Figure 4(b) shows the SHG intensity (blue squares) detected along the x axis, as the sample was rotated between $\theta = \pm 45°$ about the y axis, with the orthorhombic model fit (black line). The mathematical model for the SHG intensity for a thin film on a substrate is shown in detail in Ref. [19]. The effective nonlinear optical d coefficient for orthorhombic $mm2$ symmetry along the x direction is given by

$$d_{\text{eff}} \propto [\sin 2\theta_{\omega} \sin\theta_{2\omega} + (K_1 \cos^2\theta_{\omega} + K_2 \sin^2\theta_{\omega}) \cos\theta_{2\omega}], \quad (1)$$

where the K_1, K_2 terms are functions of the d_{ijk} tensor coefficients and θ_{ω} ($\theta_{2\omega}$) are the refractive angles for the fundamental (second harmonic) beams, respectively. Also shown in Fig. 4(b) are tilt scans for molecular beam epitaxy grown tetragonal $BFO/YAlO_3$ (orange circles), and rhombohedral $BFO/SrTiO_3$ (red triangles) thin films, with corresponding theory fits shown as black lines [20]. The generated SHG for tetragonal (4 mm) point group symmetry (out-of-plane polarization) is zero at normal incidence and symmetric, whereas for rhombohedral (3 m) point group symmetry, the SHG response is asymmetric, in clear contrast to the SHG tilt scan curve for the orthorhombic BFO.

Piezoresponse force microscopy (PFM) was employed to probe the local ferroelectricity. Using this approach, the IP ferroelectric domain structure is manifested by three contrasts, i.e., dark, bright, and intermediate, which

represent the ferroelectric components with IP polarizations toward the left, the right, and along the axis of the cantilever, respectively. As for the OOP PFM images, the dark and bright contrasts represent the upward and downward polarizations. The PFM results are summarized in Fig. 5(a). First, we noticed that the OOP image shows negligible contrast, which is attributed to the cross talk from IP measurements. The BFO thin film exhibits periodic stripelike structures (along the $[010]_{pc}$ direction) in IP measurements. Such results indicate that the $\langle 111\rangle_{pc}$ polarization directions in bulk are drastically suppressed in the $\langle 001\rangle_{pc}$ directions by the tensile strain. Careful examination of repeating the measurements with sample rotation of 90° and 180° have revealed the $\langle 110\rangle_{pc}$ IP polarizations and again confirmed the insignificant contrast in OOP PFM and the strong contrast in the IP PFM. As a result, we conclude that the polarizations lie along $\langle 110\rangle_{pc}$ directions, which is consistent with our SHG results. In order to minimize the free energy, the most stable configuration of the polarization directions in domain structures are head to tail; this suggests that the domain walls should form along $\langle 010\rangle_{pc}$, which is consistent with our PFM and TEM observations, as schematically illustrated in Fig. 5(b).

In order to interrogate both ferroelectric and antiferromagnetic (AFM) order parameters in the orthorhombic BFO phase, we employed linearly polarized soft x-ray absorption spectroscopy (XAS) and x-ray linear dichroism (XLD). XLD is the difference of the absorption of linearly polarized light, measured at a particular photon energy

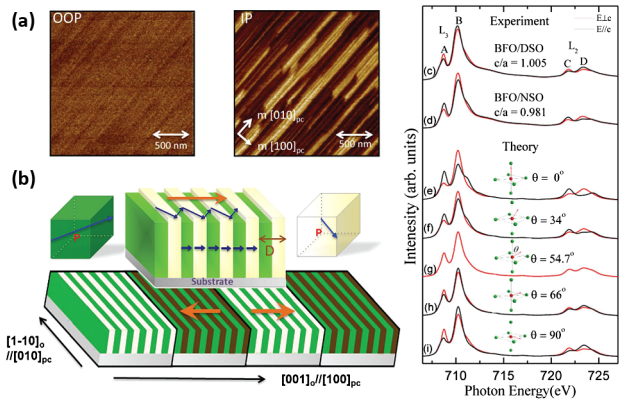

FIG. 5 (color online). PFM and x-ray absorption spectroscopy studies on orthorhombic $BiFeO_3$. (a) OOP PFM and IP PFM images obtained under a 5 V ac bias on a 15 nm thick $BiFeO_3/NdScO_3$ sample. (b) Schematic of ferroelectric domain structures of orthorhombic $BiFeO_3$. The dark gray (blue) arrows depict the ferroelectric polarization directions in each domain, while the light gray (orange) arrows show the net ferroelectric polarization. Experimental (c), (d) and theoretical (e)–(i) comparison of polarization-dependent Fe-$L_{2,3}$ spectra of $BiFeO_3/DyScO_3$ and $BiFeO_3/NdScO_3$ thin films. The gray (red) and black curves correspond to the polarization of x ray parallel to IP and OOP directions, respectively.

(e.g., corresponding to the Fe^{3+} absorption edge), with orthogonal light polarizations [21–26]. BFO thin films possess a high spin Fe^{3+} ion with a $2p^63d^5$ ground state; the polarization dependence with respect to the magnetization axis shows up as variations in the peak intensities, and the crystal field dichroism also causes the shifts in the peak positions. In addition to the orthorhombic BFO/NSO sample, a $BFO/DyScO_3$ (DSO) sample was used as the reference sample. Owing to the fact that lattice constants of BFO and DSO are very close, BFO films grown on DSO substrates are almost strain free as the ''parent rhombohedral BFO phase.' Figures 5(c)–5(i) show the XAS spectra of the Fe $L_{2,3}$ edge and their dependence on the direction of the polarization of the x ray [along the a axis [gray (red) line] or along the c axis (black line)]. The XAS peaks resulting from the L_3 edge are marked as A and B, and those resulting from the L_2 edge are marked as C and D.

We first discuss the XAS spectra of the BFO/DSO sample. When comparing the intensities of the XAS peaks at different polarization of x ray, it is found the intensities of A and C increase when the polarization of x ray is parallel to the a axis of the BFO thin film. B and D, however, show higher intensity when the polarization of x ray is parallel to the c axis. Interestingly, when conducting the same measurements on the BFO/NSO sample, completely opposite results were obtained: the intensities of A and C decrease when the polarization of x ray is parallel to the a axis of the BFO thin film, and the intensities of B and D are lower when the polarization of x ray is parallel to the c axis. This finding suggests that a rotation of the AFM axis occurs when subjected to different strain states [21,22].

To extract the orientations of theses AFM axes, we have simulated the experimental spectra using configuration interaction cluster calculations, based on atomic multiplet theory and the local effects of the solid [27,28]. It takes into account the intra-atomic $3d$-$3d$ and $2p$-$3d$ Coulomb interactions, the atomic $2p$ and $3d$ spin orbit couplings, the oxygen $2p$-$3d$ hybridization, and local crystal field interactions [29]. The simulations were carried out using the program XTLS 8.3 [27], and the parameters used are listed in Ref. [30]. Figures 5(c)–5(i) show a comparison between the experimental Figs. 5(c) and 5(d) and the simulated Figs. 5(e)–5(i) Fe-$L_{2,3}$ $E \perp c$ [gray (red) line] and $E \parallel c$ (black line) XAS spectra of BFO thin films as a function of the angle θ between the AFM axis and the c axis. From Figs. 5(e)–5(i), the angle θ is varied from 0° to 90°, i.e., rotating the magnetic moment from out-of-plane to in-plane. We found that the best agreement between theoretical and experimental spectra occurs at $\theta = 34°$ for BFO/NSO ($\theta = 66°$ for BFO/DSO) and -75 meV splitting for the e_g orbitals, reflecting a compressed distortion of FeO_6 octahedron under a tensile strain.

In summary, through a combination of theoretical and experimental methods, we demonstrate a pathway to create

and stabilize a new orthorhombic phase in multiferroic BFO thin films via strain engineering. Combined with SHG and PFM results, in-plane ferroelectric polarization is revealed in the BFO/NSO system at room temperature. XLD measurements have further discovered the rotations of the AFM axis toward the out-of-plane directions in the orthorhombic structure. This study reveals that the crystal structure has a strong influence on both ferroelectric and antiferromagnetic ordering, but also suggests the possibility of manipulating antiferromagnetic ordering with epitaxial strain in BFO system. Such an approach has opened a new scenario for us to create and manipulate a new polymorph of BFO including its altered interplay between order parameters.

We acknowledge financial support by the National Science Council, R. O. C. (NSC-101-2119-M-009-003-MY2), Ministry of Education (MOE-ATU 101W961), and Center for Interdisciplinary Science of National Chiao Tung University. The work at Berkeley is supported by the Director, Office of Science, Office of Basic Energy Sciences, Materials Sciences Division of the U.S. Department of Energy under Contract No. DE-AC02-05CH1123. V. G. acknowledges support from the National Science Foundation, Contracts No. DMR-0820404 and No. DMR-1210588. The work at Penn State is supported by DOE Basic Sciences under Grant No. DOE DE-FG02-07ER46417 (G. S. and L. Q. C.). The work at Cornell is supported by Army Research Office (ARO) Grant No. W911NF-08-2-0032.

*Corresponding author.
yhc@cc.nctu.edu.tw

[1] R. Ramesh and N. A. Spaldin, Nat. Mater. **6**, 21 (2007).
[2] J. Wang, J. B. Neaton, H. Zheng, V. Nagarajan, S. B. Ogale, B. Liu, D. Viehland, V. Vaithyanathan, D. G. Schlom, U. V. Waghmare, N. A. Spaldin, K. M. Rabe, M. Wuttig, and R. Ramesh, Science **299**, 1719 (2003).
[3] J. Wang, H. Zheng, Z. Ma, S. Prasertchoung, M. Wuttig, R. Droopad, J. Yu, K. Eisenbeiser, and R. Ramesh, Appl. Phys. Lett. **85**, 2574 (2004).
[4] F. Zavaliche, P. Shafer, R. Ramesh, M. P. Cruz, R. R. Das, D. M. Kim, and C. B. Eom, Appl. Phys. Lett. **87**, 252902 (2005).
[5] S. Y. Yang, F. Zavaliche, L. Mohaddes-Ardabili, V. Vaithyanathan, D. G. Schlom, Y. J. Lee, Y. H. Chu, M. P. Cru, Q. Zhan, T. Zhao, and R. Ramesh, Appl. Phys. Lett. **87**, 102903 (2005).
[6] R. R. Das, D. M. Kim, S. H. Baek, C. B. Eom, F. Zavaliche, S. Y. Yang, R. Ramesh, Y. B. Chen, X. Q. Pan, X. Ke, M. S. Rzchowski, and S. K. Streiffer, Appl. Phys. Lett. **88**, 242904 (2006).
[7] R. J. Zeches, M. D. Rossell, J. X. Zhang, A. J. Hatt, Q. He, C. H. Yang, A. Kumar, C. H. Wang, A. Melville, C. Adamo, G. Sheng, Y. H. Chu, J. F. Ihlefeld, R. Erni, C. Ederer, V. Gopalan, L. Q. Chen, D. G. Schlom, N. A. Spaldin, L. W. Martin, and R. Ramesh, Science **326**, 977 (2009).
[8] I. C. Infante, S. Lisenkov, B. Dupé, M. Bibes, S. Fusil, E. Jacquet, G. Geneste, S. Petit, A. Courtial, J. Juraszek, L. Bellaiche, A. Barthelemy, and B. Dkhil, Phys. Rev. Lett. **105**, 057601 (2010).
[9] J. X. Zhang, D. G. Schlom, L. Q. Chen, and C. B. Eom, Appl. Phys. Lett. **95**, 122904 (2009).
[10] J. X. Zhang, Y. L. Li, S. Choudhury, L. Q. Chen, Y. H. Chu, F. Zavaliche, M. P. Cruz, R. Ramesh, and Q. X. Jia, J. Appl. Phys. **103**, 094111 (2008).
[11] L. Q. Chen, Annu. Rev. Mater. Res. **32**, 113 (2002).
[12] A. K. Tagantsev, Ferroelectrics **375**, 19 (2008).
[13] G. Sheng and L. Q. Chen (unpublished).
[14] B. Dupé, S. Prosandeev, G. Geneste, B. Dkhil, and L. Bellaiche, Phys. Rev. Lett. **106**, 237601 (2011).
[15] B. Veličkov, V. Kahlenberg, R. Bertram, and M. Bernhagen, Z. Kristallogr. **222**, 466 (2007).
[16] See Supplemental Material at http://link.aps.org/supplemental/10.1103/PhysRevLett.109.247606 for structural nature of orthorhombic $BiFeO_3$.
[17] P. Chen, N. J. Podraza, X. S. Xu, A. Melville, E. Vlathos, V. Gopalan, R. Ramesh, D. G. Schlom, and J. L. Musfeldt, Appl. Phys. Lett. **96**, 131907 (2010).
[18] S. A. Denev, T. T. A. Lummen, E. Barnes, A. Kumar, and V. Gopalan, J. Am. Ceram. Soc. **94**, 2699 (2011).
[19] W. N. Herman and L. M. Hayden, J. Opt. Soc. Am. B **12**, 416 (1995).
[20] Y. Cong, I. An, K. Vedam, and R. W. Collins, Appl. Opt. **30**, 2692 (1991).
[21] P. Kuiper, B. G. Searle, P. Rudolf, L. H. Tjeng, and C. T. Chen, Phys. Rev. Lett. **70**, 1549 (1993).
[22] A. Scholl, J. Stohr, J. Luning, J. W. Seo, J. Fompeyrine, H. Siegwart, J. P. Locquet, F. Nolting, S. Anders, E. E. Fullerton, M. R. Scheinfein, and H. A. Padmore, Science **287**, 1014 (2000).
[23] F. Nolting, A. Scholl, J. Stohr, J. W. Seo, J. Fompeyrine, H. Siegwart, J. P. Locquet, S. Anders, J. Luning, E. E. Fullerton, M. F. Toney, M. R. Scheinfein, and H. A. Padmore, Nature (London) **405**, 767 (2000).
[24] S. I. Csiszar, M. W. Haverkort, Z. Hu, A. Tanaka, H. H. Hsieh, H. J. Lin, C. T. Chen, T. Hibma, and L. H. Tjeng, Phys. Rev. Lett. **95**, 187205 (2005).
[25] E. Arenholz, G. vanderLaan, R. V. Chopdekar, and Y. Suzuki, Phys. Rev. B **74**, 094407 (2006).
[26] N. Hollmann, Z. Hu, T. Willers, L. Bohaty, P. Becker, A. Tanaka, H. H. Hsieh, H. J. Lin, C. T. Chen, and L. H. Tjeng, Phys. Rev. B **82**, 184429 (2010).
[27] F. M. F. de Groot, J. Electron Spectrosc. Relat. Phenom. **67**, 529 (1994).
[28] A. Tanaka and T. Jo, J. Phys. Soc. Jpn. **63**, 2788 (1994).
[29] A. E. Bocquet, T. Mizokawa, K. Morikawa, A. Fujimori, S. R. Barman, K. Maiti, D. D. Sarma, Y. Tokura, and M. Onoda, Phys. Rev. B **53**, 1161 (1996).
[30] FeO_6 cluster parameters for all samples: $\Delta = 2.0$ eV, $U_{dd} = 5.0$ eV, $U_{pd} = 6.0$ eV, Slater integrals reduced to 70% of Hartree-Fock values $H_{ex} = 63$ meV.